*Article*

# Mapping Arctic Plant Functional Type Distributions in the Barrow Environmental Observatory Using WorldView-2 and LiDAR Datasets

**Zachary Langford [1,2,\*], Jitendra Kumar [1,2], Forrest M. Hoffman [3], Richard J. Norby [1,2], Stan D. Wullschleger [1,2], Victoria L. Sloan [4] and Colleen M. Iversen [1,2]**

[1] Bredesen Center for Interdisciplinary Research and Graduate Education, University of Tennessee, Knoxville, TN 37996, USA; jkumar@climatemodeling.org (J.K.); norbyrj@ornl.gov (R.J.N.); wullschlegs@ornl.gov (S.D.W.); iversencm@ornl.gov (C.M.I.)

[2] Environmental Sciences Division and Climate Change Science Institute, Oak Ridge National Laboratory, Oak Ridge, TN 37831, USA

[3] Computer Science and Mathematics Division and Climate Change Science Institute, Oak Ridge National Laboratory, Oak Ridge, TN 37831, USA; forrest@climatemodeling.org

[4] Department of Civil Engineering, University of Bristol, Bristol, UK; V.L.Sloan@bristol.ac.uk

\* Correspondence: zlangfor@vols.utk.edu; Tel.: +1-865-574-6963

**Abstract:** Multi-scale modeling of Arctic tundra vegetation requires characterization of the heterogeneous tundra landscape, which includes representation of distinct plant functional types (PFTs). We combined high-resolution multi-spectral remote sensing imagery from the WorldView-2 satellite with light detecting and ranging (LiDAR)-derived digital elevation models (DEM) to characterize the tundra landscape in and around the Barrow Environmental Observatory (BEO), a 3021-hectare research reserve located at the northern edge of the Alaskan Arctic Coastal Plain. Vegetation surveys were conducted during the growing season (June–August) of 2012 from 48 1 m × 1 m plots in the study region for estimating the percent cover of PFTs (i.e., sedges, grasses, forbs, shrubs, lichens and mosses). Statistical relationships were developed between spectral and topographic remote sensing characteristics and PFT fractions at the vegetation plots from field surveys. These derived relationships were employed to statistically upscale PFT fractions for our study region of 586 hectares at 0.25-m resolution around the sampling areas within the BEO, which was bounded by the LiDAR footprint. We employed an unsupervised clustering for stratification of this polygonal tundra landscape and used the clusters for segregating the field data for our upscaling algorithm over our study region, which was an inverse distance weighted (IDW) interpolation. We describe two versions of PFT distribution maps upscaled by IDW from WorldView-2 imagery and LiDAR: (1) a version computed from a single image in the middle of the growing season; and (2) a version computed from multiple images through the growing season. This approach allowed us to quantify the value of phenology for improving PFT distribution estimates. We also evaluated the representativeness of the field surveys by measuring the Euclidean distance between every pixel. This guided the ground-truthing campaign in late July of 2014 for addressing uncertainty based on representativeness analysis by selecting 24 1 m × 1 m plots that were well and poorly represented. Ground-truthing indicated that including phenology had a better accuracy ($R^2 = 0.75$, $RMSE = 9.94$) than the single image upscaling ($R^2 = 0.63$, $RMSE = 12.05$) predicted from IDW. We also updated our upscaling approach to include the 24 ground-truthing plots, and a second ground-truthing campaign in late August of 2014 indicated a better accuracy for the phenology model ($R^2 = 0.61$, $RMSE = 13.78$) than only using the original 48 plots for the phenology model ($R^2 = 0.23$, $RMSE = 17.49$). We believe that the cluster-based IDW upscaling approach and the representativeness analysis offer new insights for upscaling high-resolution data in fragmented landscapes. This analysis and approach provides PFT maps needed to inform land surface models in Arctic ecosystems.

## 1. Introduction

The Arctic has emerged as an important focal point for the study of climate change, with rates of recent climate warming approximately twice the global average [1]. Climate warming is projected to continue in this region with broad implications for sensitive tundra ecosystems and globally important climate feedbacks [2]. Observations also suggest that permafrost thaw is common in high-latitude ecosystems and is expected to drive changes in climate forcing through biogeochemical and biophysical feedbacks [3]. These interacting feedbacks will take place in an environment expected to undergo dramatic geomorphic change and landscape reorganization [4]. Increases in active-layer thickness at some locations have driven ecosystem responses, including changes in vegetation cover [5]. Changes in vegetation community composition and distribution can affect albedo and energy partitioning in the Arctic [5,6]. Furthermore, recent studies indicate that the phenology of vegetation (the timing of processes throughout the growing season) is a primary indicator of the dynamic responses of terrestrial ecosystems to climate change [7].

Terrestrial vegetation plays an important role in the dynamics of the Earth system through water and energy exchange and is one of the largest sources of uncertainty in climate change predictions [8]. In the Accelerated Climate Model for Energy (ACME) land model (ALM), as with most other models [8], vegetation is not represented as biomes, but rather as plant functional types (PFTs) [9]. Each PFT groups plant species that share similar responses to environmental factors and effects on ecosystems [10,11]. Most climate models currently use only two PFTs (one grass and one shrub type) to represent Arctic vegetation, greatly limiting the representation of plant functions and feedbacks in simulating Arctic responses to a warming climate [9]. Chapin et al. [12,13] recommended the use of Arctic- and boreal-specific PFTs in vegetation models, including deciduous shrubs, evergreen shrubs, sedges, grasses, forbs, *Sphagnum* moss, non-*Sphagnum* moss and lichens, to capture Arctic vegetation processes.

Poulter et al. [14] showed that accurate PFT datasets are important for reducing the uncertainty of terrestrial biogeochemical processes to climate variability in Earth system models. Satellite datasets have been used to extract PFT information from the landscape and can contribute to improved predictive capabilities of land-atmosphere interactions [15]. Different remote sensing-based PFT products are available for Earth system models [11,14,16]. However, these products for parameterizing PFTs are at a coarse resolution (hundreds of meters to kilometers). New high resolution products are needed to capture the fine-scale heterogeneity of PFTs observed in the field.

There is a growing interest in understanding and resolving the subgrid scale processes in heterogeneous Arctic ecosystem. The U.S. Department of Energy's Office of Science Next Generation Ecosystem Experiments (NGEE) Arctic project seeks to couple high-resolution models to Earth system models to represent Arctic land surface and subsurface processes and their interactions in a warming climate, such as high-resolution hydrologic (e.g., Arctic Terrestrial Simulator, PFLOTRAN ) [17,18] , biogeochemical (PFLOTRAN) [19] and biosphere models (CLM-PFLOTRAN) [19], can run at fine spatial and temporal resolutions and require high-resolution datasets. This need for parameterizing high-resolution land surface models require new approaches for developing such high-resolution products.

Most optical remote sensing studies of Arctic vegetation consist of coarse resolution datasets from 30 m–250 m [15,20,21], and few studies have been performed at the WorldView-2 resolution (∼0.5–∼2 m) [22]. Medium resolution satellite datasets are useful for characterizing PFT coverage at regional to global scales, but there are challenges to integrating such datasets with sparse small-scale point measurements for upscaling. WorldView-2 multispectral satellite imagery has a much higher spatial resolution and can help capture the fine-scale variation in PFTs.

There has been considerable recent progress in the development of methods for handling and analyzing high-resolution remote sensing data. Dalmayne et al. [23] used WorldView-2 satellite spectral dissimilarity to infer environmental heterogeneity in dry semi-natural grasslands, which revealed a significant positive association between spectral dissimilarity and fine-scale plant species beta diversity. Ramoelo et al. [24] monitored leaf N and above-ground biomass as an indicator of rangeland quality and quantity using WorldView-2 satellite images and the random forest technique. Karna et al. [25] integrated WorldView-2 satellite images with small footprint airborne LiDAR data for estimation of tree carbon at the species level. Mutanga et al. [26] demonstrated the utility of WorldView-2 imagery and random forest regression in estimating and mapping vegetation biomass at high density. Gangodagamage et al. [27] used LiDAR and WorldView-2 data to show variability in active layer thickness and the controls of local microtopography in Barrow, AK. These studies suggest that high spatial resolution data, such as WorldView-2 and LiDAR data, may potentially contribute to the development of improved methods for the mapping and monitoring of vegetation at fine scales and use for high-resolution land surface models.

Phenology, seasonal changes in plants from year to year, can be a useful proxy for monitoring vegetation [28]. Remote sensing phenology studies use data gathered by satellite sensors that measure wavelengths of light absorbed and reflected by green plants. Several remote sensing studies of phenology use satellites to track seasonal changes in vegetation on regional, continental and global scales [29,30]. However, very few studies have used high-resolution (e.g., WorldView-2/3) image time series for understanding seasonal patterns in reflectance that can enable the detection and change of vegetation at fine spatial scales. It is important to develop analysis techniques to capitalize on rich time series of imagery from high-resolution sensors as they become more available. In this study, we hypothesize that capturing the vegetation phenology using repeat imagery from high-resolution satellite data will help improve the characterization of the PFT distributions at our study site.

In situ field measurements are made at relatively few and specific geographic points and are representative samples of regions of similar characteristics. To upscale the in situ field measurements at larger scales for estimating landscape-scale characteristics, the representativeness of those measurements must be quantified. A representativeness metric provides insight into coverage provides by the field samples, the selection of optimal sampling locations and offer a quantitative approach for down-scaling of remote sensing data and extrapolation of measurements to unsampled domains [31]. Sampling in under-represented sites, guided by the representativeness metric, can lead to improved accuracy in the upscaling of the measured quantity (PFTs in current study).

The objectives of this study are to: (1) characterize the landscape using high-resolution multi-spectral WorldView-2 satellite imagery and LiDAR-derived DEM; (2) use an interpolation algorithm for upscaling vegetation surveys and creating gridded PFT datasets based on remote sensing imagery; (3) use salient differences in growing season phenology (timing and magnitude of greenness) to help discriminate among various PFTs; (4) quantify the uncertainty in gridded estimates of PFT distributions upscaled from point observations using a representativeness metric; (5) devise optimal sampling strategies for ground-truthing and to improve PFT estimates and reduce uncertainty.

Interpolation is a process of using measurements about a process at a limited number of point locations to make estimates about the process at other, unmeasured locations. In this study, the term upscaling is defined as an interpolation process to employ point measurements to develop gridded estimates. An important objective was to develop a new data analytic approach to mine high resolution spectral remote sensing datasets for signatures of surface vegetation to develop estimates of PFT distributions at high spatial resolution (0.25 m × 0.25 m) across a fragmented Arctic landscape.

## 2. Methodology

The Methodology section follows the structure shown in Figure 1. Section 2.1 describes the study sites (Section 2.1.1), field vegetation surveys (Section 2.1.2) and the remote sensing datasets used in this study (Section 2.1.3). The *k*-means algorithm for stratifying the heterogeneous landscape

using remote sensing datasets is described in Section 2.2. Section 2.3 describes the methodology to quantify the representativeness of the field vegetation surveys in the context of the larger study region. Section 2.4 presents the approach for statistically upscaling the PFT distribution on the landscape using the clusters from Section 2.2. Section 2.5 describes the approach for the validation of the upscaled PFT distributions using a bootstrapping approach (Section 2.5.1) and on the ground via additional field surveys (Section 2.5.2).
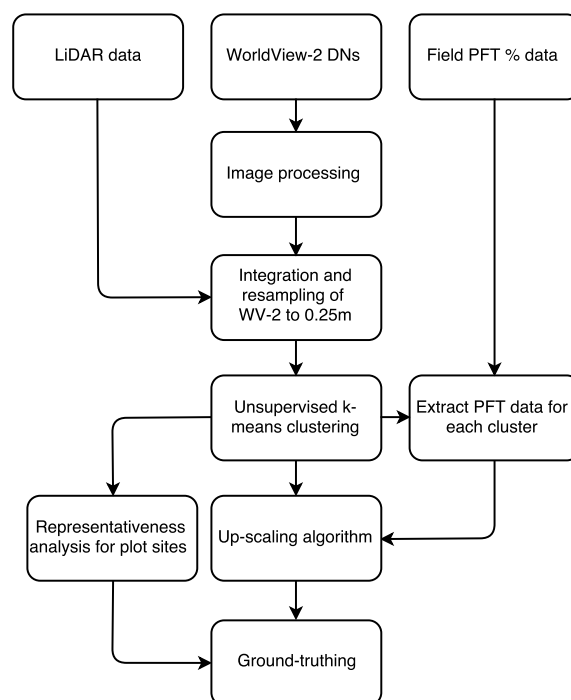
**Figure 1.** Flowchart of the methods used in this study.

*2.1. Study Area and Datasets*

2.1.1. Study Area

The study area is located within the Barrow Environmental Observatory (BEO) located 6 km east of Barrow, Alaska (71.3°N, 156.5°W), as part of the U.S. Department of Energy's Office of Science Next Generation Ecosystem Experiments (NGEE) Arctic project (Figure 2). The NGEE Arctic project seeks to reduce uncertainty in climate prediction by better understanding critical land–atmosphere feedbacks in terrestrial ecosystems of Alaska. NGEE Arctic has established four 100 m × 100 m intensively-sampled areas (Figure 2A–D; Table 1) within the BEO. The mean annual air temperature is −12 °C, and the mean temperature from June–August is 3.2 °C [32]. The annual adjusted precipitation is 173 mm·year$^{-1}$ [32], with the majority of precipitation falling during the summer months. Soils on the BEO are generally classified as Gelisols, which are characterized by an organic-rich surface layer underlain by a horizon of silty clay to silt-loam textured mineral material and a frozen organic-rich mineral layer. The seasonally-active-layer thickness ranges between 30 and 90 cm at the BEO [33,34].
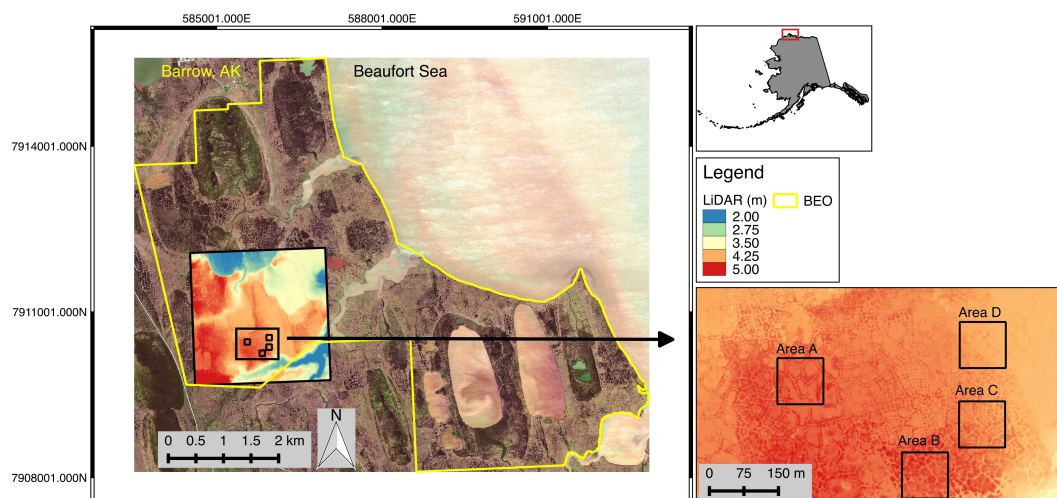
**Figure 2.** Natural-color composite WorldView-2 image from 3 August 2010, showing the study area within the Barrow Environmental Observatory (BEO) (yellow) and the LiDAR data extent for sampling Areas A, B, C and D. The spatial extent of each sampling area is 100 m × 100 m. NextView License ©2016 DigitalGlobe.

The BEO is a low relief landscape, with <7-m differences in topography (Figure 2) and a low hydraulic gradient region characterized by thaw lakes and drained basins [35]. Seasonal freeze and thaw processes have produced a polygonal network of high centered polygons, low centered polygons and transitional polygons [36]. Table 1 lists the polygonal characteristics for Areas A–D.

**Table 1.** Area A, B, C and D polygonal features and environmental characteristics.

| Area | Characteristics | Relative Elevation | Moisture Conditions |
| --- | --- | --- | --- |
| A | Low center polygons (with edges and troughs) | Low | Inundated |
| B | High center polygons | High | Desiccated |
| C | Transitional low center polygons (with edges and troughs) | Moderate | Moderately Dry |
| D | Low center polygons (few edges and troughs) | Low | Inundated |

### 2.1.2. Field Vegetation Surveys

Plant community surveys were undertaken at 48 permanently marked 1 m × 1 m plots in and around the four NGEE Arctic sites (12 plots for Areas A, B, C and D) dominated by differing polygon types (Table 1; Figure 2). Plots were located in homogeneous vegetation communities in the centers, edges and troughs of four polygons per area and the locations of the plot corners surveyed using dGPS. Aerial fractional coverages of all vascular, bryophyte and lichen species or genera and bare ground were visually estimated by a single surveyor between 17 July and 29 July 2012. Rare species were assigned nominal values of 0.1% (single individual), 1% (multiple individuals) and 3% (few individuals forming <5% coverage) and all remaining species recorded to the nearest 5%. Canopies were considered to have two layers, with taller vascular plant coverage of up to 100% and a ground layer including some or all of mosses, lichens, prostrate vascular plants and bare ground with coverage of up to 100%. Standing water was not present in any plots at the time of the survey, although in polygon troughs, moss and sedge vegetation was "floating" on saturated soil. Recorded species were assigned to PFTs using the descriptions of Chapin et al. [13], with the "grass" category modified here to "wet tundra graminoids" (to include true grasses, such as *Dupontia fisheri*) and the "sedge" category to "dry tundra graminoids" (to include *Luzula* spp.). Fractional coverage of any PFT was the sum of all species in that category. Shrubs (deciduous and evergreen) were a very small component (mean of 1.27% for Areas A, B, C and D) of the plant community composition across the study region and were thus omitted in this analysis.

### 2.1.3. Remote Sensing Datasets

We used cloud-free WorldView-2 satellite (DigitalGlobe) multispectral imagery ($\sim$2 m resolution) provided by the Polar Geospatial Center (PGC). The imagery was radiometrically corrected by DigitalGlobe and orthorectified by the PGC. We assume the geolocational error to be minimal, but some errors may be possible. We analyzed the blue (450–510 nm), green (510–581 nm), red (630–690 nm) and near-infrared (NIR) (770–895 nm) bands. Images from 6 different days during the 2010 growing season (10 June, 24 June, 21 July, 26 July, 3 August and 4 August) were acquired to capture the vegetation phenology.

The 0.25-m spatial resolution LiDAR digital elevation model (DEM) used in this study was developed by AeroMetric, now known as Quantum Spatial, Inc., and flown on 4 October 2005. The DEM pixel values represent the ground elevation above sea level, with elevation values ranging from 0.00–7.06 m (mean 3.82 m). The DEM pixels show a mean difference of 0.003 meters (median = 0.004, *RMSE*= 0.043 m) compared to survey data (*n* = 286 points) collected in August 2006. More information on the LiDAR dataset can be found at http://dx.doi.org/10.5065/D6KS6PQ3. We assumed that the spatial variability of PFTs during WorldView-2 and LiDAR image collection in 2010 and 2005, respectively, was similar to the field surveys conducted during 2012 for the comparison of remotely-sensed data with field observations.

We converted all WorldView-2 imagery to top-of-atmosphere (TOA) reflectance. TOA reflectance is the reflectance measured by the space-based sensor flying higher than the Earth's atmosphere. TOA reflectance does not account for topographic, atmospheric or bidirectional reflectance distribution function (BRDF) differences. The pixel digital numbers (DNs) were converted to top-of-atmosphere band-averaged reflectance according to Updike and Comp [37].

A commonly-used index for the estimation of vegetation properties using satellite remote sensing is the normalized difference vegetation index (NDVI). NDVI is based on the contrast between absorption in the red band by chlorophyll pigments and reflectance in the NIR band caused by internal scattering within leaves [38]. NDVI calculated from different WorldView-2 satellite bands has been used for the estimation of fine-scale species diversity in semi-natural grasslands [23]. NDVI was calculated as:

$$\text{NDVI} = \frac{\rho_{\text{nir}} - \rho_{\text{red}}}{\rho_{\text{nir}} + \rho_{\text{red}}} \tag{1}$$

where $\rho_{\text{red}}$ and $\rho_{\text{nir}}$ stand for the TOA reflectance measurements acquired in the red and NIR regions, respectively. TOA reflectance values vary between 0.0 and 1.0; thus, NDVI varies between $-1.0$ (no vegetation) and $+1.0$ (green vegetation).

The WorldView-2 datasets were resampled to the LiDAR resolution of 0.25 m $\times$ 0.25 m, using the nearest-neighbor resampling algorithm. The spectral and topographic characteristics were extracted from the remote sensing datasets at the corners of the 48 field plots (192 plot corners) using Global Positioning System (GPS) coordinates. The spectral (WorldView-2) and topographic (LiDAR) characteristics varied on scales as small as 0.25 m $\times$ 0.25 m, and thus, each of the 48 field vegetation plots can encompass multiple fine-scale topographic properties (Figure 3c). To preserve and capture this heterogeneity, the PFT% values were extracted at the 192 plot corners. The PFT fraction used in the upscaling model consisted of percent averages for the 1 m $\times$ 1 m plot (Figure 3d). The resampling of WorldView-2 and extraction of remote sensing data at the plot corners allowed for evaluating the topographic controls on the PFT upscaling.
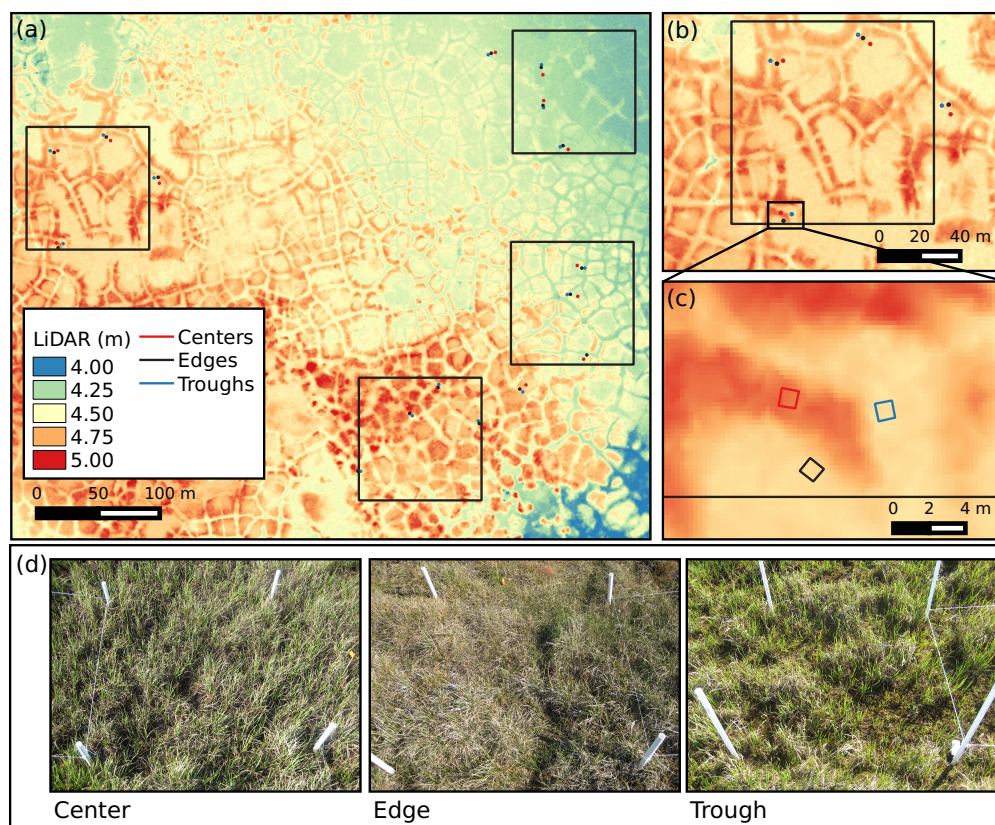
**Figure 3.** (**a**) Location of vegetation plots for sampling Areas A–D; (**b**) Area A vegetation plots; (**c**) showing the sampling by the polygonal features centers, edges and troughs; (**d**) field photos taken during the sampling campaign in late July 2012 for a center (left), edge (middle) and trough (right). The center plot consisted of 48.8% wet tundra graminoids, 5% mosses and 47.5% bare ground. The edge plot consisted of 59.8% wet tundra graminoids, 11.5% dry tundra graminoids, 2% forbs, 9.7% lichens, 25% mosses and 21.3% bare ground. The troughs consisted of 24% wet tundra graminoids and 85% mosses.

## 2.2. Characterizing the Heterogeneous Landscape

Complex geomorphology, hydrology and biogeochemistry in the Arctic landscape leads to a highly heterogeneous distribution of vegetation on the landscape. These heterogeneities are captured by remote sensing as spectral responses of the vegetation. We characterize the landscape using remote sensing datasets to identify regions of similar characteristics. The classification of landscape would in turn allow the development of accurate and specialized statistical models for the upscaling of PFT distributions.

We used a *k*-means algorithm for stratification of the landscape using WorldView-2 and LiDAR datasets. Landscape classes determined by the algorithm, not directly used in upscaling process (Section 2.4), were only used as subregions for developing customized statistical upscaling model. The *k*-means algorithm clusters a dataset $(\vec{X}_1, \vec{X}_2, \ldots, \vec{X}_n)$ with *n* records into a desired number of clusters, *k*, equalizing the full multi-dimensional variance across clusters [39]. The number of clusters, *k*, is supplied as an input and remains fixed. The *k*-means algorithm starts with initial centroid vectors $(\vec{C}_1, \vec{C}_2, \ldots, \vec{C}_k)$ and calculates the Euclidean distance of each pixel $(\vec{X}_i, 1 \leq i \leq n)$ to every centroid $(\vec{C}_j, 1 \leq j \leq k)$, classifying it to the closest existing centroid. The centroid vector is recalculated as the vector mean of all dimensions of each pixel assigned to that centroid. This classification and re-calculation process is iteratively repeated until fewer than some fixed proportion of observations changes their cluster assignment between iterations. For this study, convergence was assumed once fewer than 0.05% of the observations change cluster assignments between two iterations.

Hoffman et al. [40] developed a parallel version of the *k*-means algorithm to accelerate convergence, handle empty cluster cases and obtain initial centroids through a scalable implementation of the Bradley and Fayyad [41] method. Kumar et al. [42] extended this to a fully-distributed and highly scalable parallel version of the *k*-means algorithm for analysis of very large datasets, which was used in this study.

One of the key hypotheses in this study was that phenology would help discriminate among various PFTs through salient differences in timing and magnitude of greenness (NDVI) during the growing season. To test this hypothesis, two sets of analyses were conducted, with and without phenology. The with phenology case used a set of 31 characteristics at 0.25 m × 0.25 m resolution (Table 2). The characteristics included the blue, green, red, near-infrared bands and NDVI for the six snapshots from WorldView-2 during the growing season and the LiDAR elevation values. We found the LiDAR elevation values to be sufficient enough for capturing the microtopography effects on PFT patterns, and thus, we do not include other LiDAR metrics (e.g., slope and aspect) in the analysis.

For the without phenology case, a single WorldView-2 snapshot image from 21 July 2010 (middle of the growing season) that consisted of 6 characteristics (blue, green, red, near-infrared bands, NDVI and LiDAR) was used. Both datasets were standardized, such that each variable had a mean of zero and a standard deviation of one prior to clustering to equalize the contribution from each predictor variable. The remainder of the paper will refer to the multi-image analysis as "with phenology" and the analysis from a single image as "without phenology". The *k*-means clustering was performed on both sets of data to stratify the landscape at various levels of divisions (3–10). This was done for evaluating the uncertainty associated with clusters and the upscaling algorithm.

**Table 2.** The 6 and 31 characteristics used in the *k*-means clustering algorithm for the without and with phenology classification, respectively.

| | Number of Variables | |
|---|---|---|
| **Variables** | (*Without Phenology, With Phenology*) | **Platform** |
| Elevation | 1, 1 | LiDAR |
| TOA Red Band | 1, 6 | WorldView-2 |
| TOA Blue Band | 1, 6 | WorldView-2 |
| TOA Green Band | 1, 6 | WorldView-2 |
| TOA NIR Band | 1, 6 | WorldView-2 |
| NDVI | 1, 6 | WorldView-2 |

## 2.3. Quantifying the Representativeness of Field Vegetation Observations

To statistically quantify the representativeness of field vegetation observations collected at the permanent plots at our site, we employ a representativeness metric described by Hargrove et al. [43] and Hoffman et al. [31] that provides a unit-less, relative measure of the dissimilarity and similarity in the multi-variate data space between any two locations of interest. The representativeness metric was calculated for both the with phenology and the without phenology analysis (Table 2). This representativeness metric captures the full range of heterogeneity in the combinations of spectral and topographic conditions, providing a continuously-varying measure of dissimilarity for every map cell with respect to any other map cell of interest. The representativeness metric is calculated as the Euclidean distance between field sampling location and any map cell/location of interest in the standardized *n*-dimensional state space. Areas with similar combinations of spectral and elevation characteristics will have a small Euclidean distance, representing a low dissimilarity value. Areas with very different combinations of characteristics will have a large Euclidean distance between them and will have high dissimilarity values. The resulting map of representativeness quantifies, in multi-variate data space (Table 2), how well the set of field samples capture the heterogeneous landscape.

*2.4. Statistical Upscaling of PFT Distribution on the Landscape*

Establishing relationships between remotely-sensed data and in situ observations can help extrapolate process understanding. Kriging-based extrapolation techniques have been widely used; however, Arctic landscapes are often spatially fragmented due to geomorphological properties, rendering such methods not applicable. We were interested in an interpolation algorithm that used sparse, irregularly-scattered data over a multidimensional domain, such as inverse distance weighting (IDW). In IDW, the interpolating function is expressed as a weighted average of the data values, where the weights are inverse functions of the distances from the PFT sites in multi-dimensional data space. In an inverse interpolation scheme, an interpolated value is calculated as:

$$\hat{z}(u) = \sum_{u_i \in \mathcal{N}(u)} w_i z(u_i) \tag{2}$$

where $\hat{z}$ represents the predicted PFT value, $w_i$ represent weights, $z(u_i)$ is the input PFT percentages and variables listed in Table 2 and $\mathcal{N}(u)$ represents the neighborhood around $u$. $\mathcal{N}(u)$ can encompass the entire space, so that all input samples contribute to the interpolated value. In IDW, the weights are set to:

$$w_i = \frac{\gamma}{d_i(u)^2} \tag{3}$$

where $\gamma$ is a normalization value chosen such that $\sum w_i = 1$ and $d_i(u)$ is the Euclidean distance between $u$ and $u_i$. The inverse interpolation scheme guarantees that each point in the output grid is assigned a predicted value [44].

We assumed that the *k*-means clustering can accurately stratify the fragmented landscape. In the IDW algorithm, $\mathcal{N}(u)$ was defined as the members of a given cluster, *k*, which uses input samples within the cluster (Table 3). That is, if $\bar{u}_k$ represents the mean state of cluster k, then $\mathcal{N}(\bar{u}_k)$ is the set of all points $u_i$ included in cluster *k*. We believe that the landscape characterization performed by *k*-means clustering will lead to a better upscaling product when using the sampling points within each cluster. For example, using only the samples in the cluster that were associated with centers can lead to a better classification of PFTs associated with this polygonal type (Figure 3 d).

The IDW model was used for estimating wet tundra graminoids, dry tundra graminoids, forbs, mosses, lichens and bare ground. For the upscaled PFTs, percent cover greater than 100% refers to plot areas that have multiple layers of PFTs, while percent cover less than 100% refers to areas that have some cover of standing water or standing dead vegetation. The upscaled PFTs were rescaled to 100% and marked as standing water or standing dead vegetation for areas under 100%. The appendix describes how standing water was detected in the WorldView-2 satellite images and the associated impacts on the upscaled estimations.

**Table 3.** The number of vegetation samples that were partitioned by the *k* clusters, with the top *k* values representing the cluster number when setting the initial *k* values from 3–10 (left column).

| *k* | Cluster Number | | | | | | | | | |
|---|---|---|---|---|---|---|---|---|---|---|
| | **1** | **2** | **3** | **4** | **5** | **6** | **7** | **8** | **9** | **10** |
| 3 | 116 | 1 | 75 | – | – | – | – | – | – | – |
| 4 | 115 | 1 | 76 | 0 | – | – | – | – | – | – |
| 5 | 79 | 68 | 44 | 0 | 1 | – | – | – | – | – |
| 6 | 0 | 0 | 63 | 49 | 79 | 1 | – | – | – | – |
| 7 | 54 | 50 | 1 | 65 | 0 | 22 | 0 | – | – | – |
| 8 | 0 | 22 | 0 | 54 | 1 | 65 | 50 | 0 | – | – |
| 9 | 0 | 55 | 51 | 45 | 4 | 18 | 19 | 0 | 0 | – |
| 10 | 33 | 26 | 0 | 1 | 50 | 0 | 0 | 10 | 54 | 18 |

*2.5. Validation of PFT Upscaling*

2.5.1. Bootstrap Validation

IDW was performed on $k = 3 \ldots 10$ for the with phenology and without phenology classifications. Bootstrap (random sampling) validation was used in order to evaluate how well IDW performed, which is essential due to the strong autocorrelation at the sampling location. Bootstrapping creates an unbiased set, where every possible combination of sampling units has an equal and independent chance of being selected. Forty eight random samples (25% of the plot corners) for wet tundra graminoids, dry tundra graminoids, forbs, mosses, lichens and bare ground (total of 288 samples) were taken out for running IDW for $k = 3 \ldots 10$. This was performed for both the without phenology and with phenology cases. To allow for fair comparison, the same set of randomly-selected points was used for the validation of both the cases. After running the IDW model, the estimated PFT values at the 48 held back locations were extracted and compared against the observation.

2.5.2. Ground-Truthing

In addition to bootstrapping validation, an independent on-ground validation was performed by conducting a field survey on 29 July 2014. The locations for field samples were strategically selected based on the representativeness analysis (Section 2.3). Within each sampling area (A, B, C and D), three locations that were well-represented by the original field samples (determined by representativeness metric) were selected for field sampling. In addition, we also selected three locations at each of the four areas that were under-represented by the original vegetation samples. Thus, a total of 24 1 m $\times$ 1 m plots was selected for field sampling for the validation of the upscaled PFT distribution products. High-resolution optical imagery was used to visually locate and extract plot coordinates across the various sampling areas. Similar to the 48 1 m $\times$ 1 m plots, the 24 plots were surveyed using a dGPS. Unlike the earlier survey of the vegetation composition, no attempt was made to identify species or genera, and only PFT measurements were made. Fractional area distributions of wet tundra graminoids, dry tundra graminoids, forbs, mosses and lichens were determined in these 24 1 m $\times$ 1 m plots. All plots were sampled close to the peak growing season.

We expect the accuracy of the estimated PFT distributions at the plots well-represented by the vegetation samples to be better compared to the plots that were under-represented. The representativeness metric helps identify the areas where additional observation can help improve the model. To test that hypothesis, we added the observation at 24 well- and under-represented plots to the IDW model training datasets and repeated the analysis to generate a new estimate of the PFT distribution. A second ground-truthing campaign was performed on 30 August 2014 at the same 24 plots using the same sampling strategy. Some senescence may have occurred by 30 August; however, it has been shown that the production of foliage can continue into late August in Barrow, AK [45]. The second ground-truthing serves to evaluate the estimation error when additional observations at well- and under-represented plots are included in the model development based on the field campaign on 29 July 2014.

## 3. Results

*3.1. Analysis of Datasets*

While the without phenology case used six variables, 31 variables were used for the with phenology case (Table 2), significantly increasing the degrees of freedom and complexity of the model. We wanted to test the significance of adding extra variables (with phenology) to verify the benefit of added complexity. The without phenology and with phenology WorldView-2 variables (Table 2) were statistically compared to the field PFT data. The 192 points for the without phenology ($n = 1152$) and with phenology ($n = 5952$) were compared using multiple linear regression and Akaike

information criterion (AIC). Table 4 shows the $R^2$, adjusted $R^2$ and AIC for the without phenology and with phenology datasets on the PFT field data. All PFTs for the with phenology dataset shows higher $R^2$ and adjusted $R^2$ and lower AIC. This gave us justification for using 31 variables in the IDW model.

**Table 4.** The $R^2$, adjusted $R^2$ and Akaike information criterion (AIC) performed on the field data and the WorldView-2 spectral characteristics.

| PFT% | Without Phenology | | | With Phenology | | |
|---|---|---|---|---|---|---|
| | $R^2$ | Adjusted $R^2$ | AIC | $R^2$ | Adjusted $R^2$ | AIC |
| Wet Tundra Graminoid | 0.13 | 0.10 | 1575.00 | 0.58 | 0.50 | 1483.80 |
| Dry Tundra Graminoid | 0.34 | 0.32 | 1305.38 | 0.59 | 0.51 | 1263.48 |
| Forb | 0.26 | 0.23 | 1401.60 | 0.48 | 0.39 | 1380.26 |
| Moss | 0.26 | 0.24 | 1754.93 | 0.53 | 0.44 | 1717.31 |
| Lichen | 0.54 | 0.53 | 1393.88 | 0.75 | 0.70 | 1329.56 |
| Bare Ground | 0.37 | 0.35 | 1619.66 | 0.63 | 0.57 | 1563.31 |

Field vegetation observations collected in 2012 demonstrate a significant spatial variability in distribution of PFTs across the polygonal types and microtopographic locations. Wet tundra graminoids were most common in Area A, while mosses were most common in Area D (Table 5). Table 5 shows the mean and standard deviations of PFT fractions for Areas A, B, C and D by polygonal feature (centers, edges and troughs). Certain PFTs were most common in certain polygonal features. For example, forbs were most common in Area C troughs, and dry tundra graminoids were most common in Area B centers. Analysis of NDVI values between 10 June 2010 and 3 August 2010 showed similar differences by polygonal feature for Areas A, B, C and D. Overall, lower NDVI values were associated with Area A, and higher NDVI values were associated with Area C. This could be because of the moisture conditions (wet Area A vs. moderately dry Area C) (Table 1), which drives the distribution of PFTs on the landscape.

**Table 5.** The mean and standard deviations of observed plant functional type (PFT) distributions at Areas A, B, C and D by polygonal feature (i.e., centers, edges and troughs).

| PFT | Centers | Edges | Troughs |
|---|---|---|---|
| | $M, SD$ | $M, SD$ | $M, SD$ |
| **Wet Tundra Graminoids** | | | |
| Area A | 33.8, 12.1 | 45.2, 12.0 | 35.0, 7.8 |
| Area B | 2.6, 2.3 | 16.1, 11.0 | 24.2, 7.1 |
| Area C | 35.8, 21.0 | 10.7, 10.0 | 21.0, 12.1 |
| Area D | 25.5, 3.7 | 23.9, 7.9 | 35.8, 13.6 |
| **Dry Tundra Graminoids** | | | |
| Area A | 0.0, 0.0 | 6.0, 4.4 | 0.0, 0.0 |
| Area B | 23.3, 12.3 | 9.3, 5.1 | 2.1, 3.8 |
| Area C | 10.5, 12.6 | 13.7, 6.3 | 1.4, 1.2 |
| Area D | 2.5, 5.0 | 2.7, 1.9 | 0.2, 0.2 |
| **Forbs** | | | |
| Area A | 0.0, 0.0 | 3.3, 3.2 | 1.3, 2.6 |
| Area B | 1.5, 2.8 | 5.3, 5.8 | 11.0, 21.2 |
| Area C | 4.0, 2.7 | 9.0, 6.0 | 17.6, 22.1 |
| Area D | 2.3, 2.6 | 16.8, 11.0 | 1.3, 1.4 |

**Table 5.** *Cont.*

| PFT | Centers M, SD | Edges M, SD | Troughs M, SD |
|---|---|---|---|
| **Mosses** | | | |
| Area A | 10.2, 5.3 | 48.1, 16.1 | 73.3, 18.6 |
| Area B | 19.0, 15.7 | 45.6, 7.1 | 53.3, 29.7 |
| Area C | 27.1, 22.0 | 61.3, 16.9 | 72.8, 20.8 |
| Area D | 41.0, 27.0 | 66.1, 14.1 | 73.2, 10.4 |
| **Lichens** | | | |
| Area A | 0.0, 0.0 | 16.4, 9.4 | 0.1, 0.1 |
| Area B | 37.3, 4.2 | 28.5, 7.2 | 1.2, 2.5 |
| Area C | 3.3, 1.8 | 16.3, 9.4 | 0.0, 0.0 |
| Area D | 0.1, 0.1 | 3.4, 4.6 | 0.0, 0.0 |
| **Bare Ground** | | | |
| Area A | 57.2, 10.0 | 5.3, 10.6 | 10.0, 14.1 |
| Area B | 14.3, 13.2 | 6.5, 5.7 | 15.3, 25.1 |
| Area C | 25.6, 15.3 | 8.1, 9.6 | 3.1, 6.2 |
| Area D | 30.6, 29.9 | 3.4, 3.7 | 1.5, 3.1 |

$M$ = mean, $SD$ = standard deviation; wet tundra graminoids include *Dupontia fisheri*, and dry tundra graminoids include *Luzula spp.*; polygonal types: Area A: low centered polygon; Area B: high center polygons; Area C: low centered polygon; Area D: low center polygons.

## 3.2. Landscape Characterization Using Unsupervised Clustering

Unsupervised clustering was applied to the multi-variate datasets for with phenology and without phenology cases to stratify the landscapes at various levels of divisions ($k = 3\ldots10$). Bootstrap validation was performed for both the without phenology and with phenology cases (as described in Section 2.5.1). IDW models for estimating PFT distributions were developed for both with phenology and without phenology cases at each level of stratification ($k = 3\ldots10$), and they showed consistent coefficients of determination ($R^2$) ranging from 0.70–0.77.

The level of division of $k$ = 6 (landscape stratified in six types) upscaled PFT distributions of wet tundra graminoids, dry tundra graminoids, forbs, mosses, lichens and bare ground had the highest $R^2$ value for with phenology (0.77) and without phenology (0.76) cases using the bootstrapping validation ($n = 288$). The choice of $k$ = 6 was used for the remainder of the analysis presented in the paper.

Our results show that the patterns in the field-based distributions (Table 5) and the spectral variables used in the IDW model (Table 2) are significantly correlated with the polygonal features. The $k$-means clustering-based ($k$ = 6) stratification of the landscape captured the polygonal microtopography well (Figure 4), as demonstrated by the high correlation achieved during bootstrap validation ($k$ = 6). For example, spectral characteristics of mosses may vary strongly between the polygon trough and edge, which would be delineated by topographic characteristics.
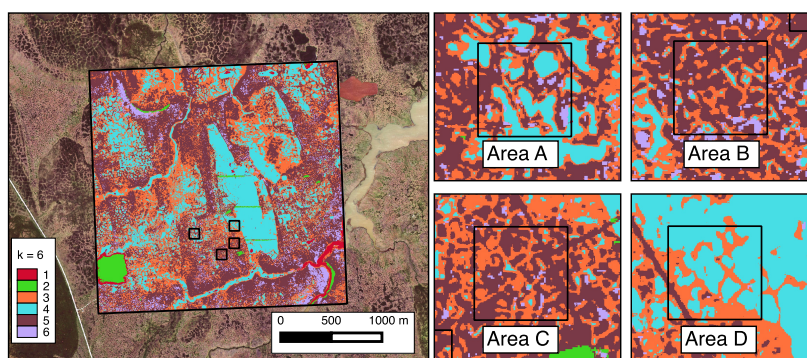
**Figure 4.** The clustering-based stratification of the landscape (*k* = 6) for the with phenology case for Areas A, B, C and D at 0.25-m resolution.

### *3.3. Upscaling of PFT Distributions*

We developed and applied the IDW model to upscale/estimate the distribution of PFT fractions across the footprint covered by the LiDAR data with a primary focus on Areas A, B, C and D, each having an area of 0.01 km$^2$. Figure 5 shows the distribution density of all PFTs within Areas A, B, C and D (160,000 pixels) for the with phenology case. The IDW model (for with phenology ) estimated that mosses had the highest percent cover for Areas A, B, C and D compared to other PFTs with mean values of 44.7%, 46.9%, 48.9% and 55.8%, respectively.
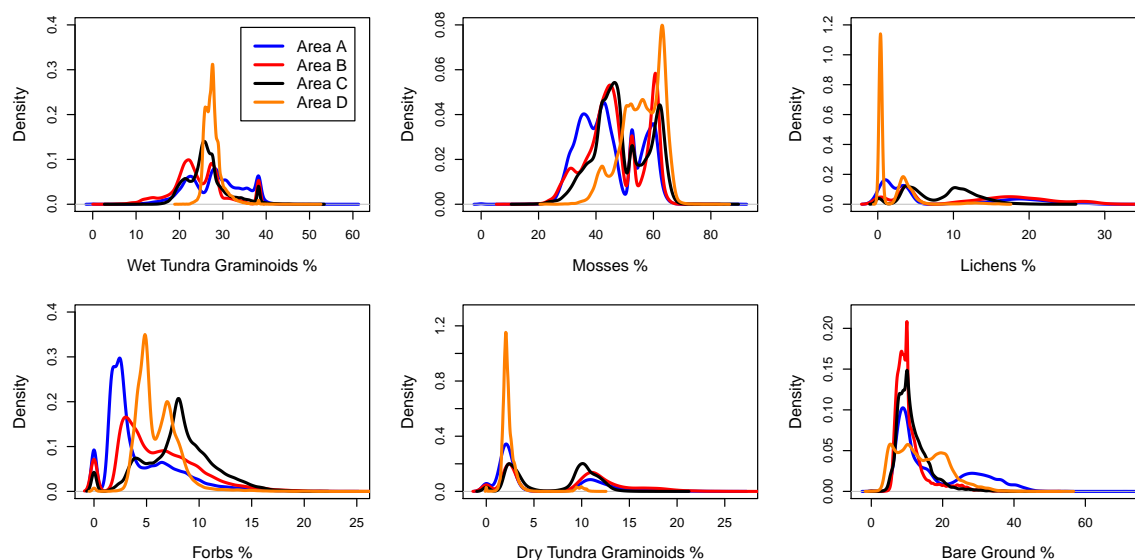


**Figure 5.** Density of PFT distributions for the with phenology case within sampling Areas A (blue), B (red), C (black) and D (orange).

Wet tundra graminoids had the second highest percent cover for Areas A, B, C and D with mean values of 28.3%, 24.1%, 26.3% and 27.6%, respectively. Bare ground had mean values of 17.5%, 10.8%, 11.6% and 14.3% for Areas A, B, C and D, respectively. Lichens had mean values of 7.9%, 12.5%, 8.4% and 2.1% for Areas A, B, C and D, respectively. Forbs had the lowest mean values of 4.3%, 6.1%, 8.1% and 6% for Areas A, B, C and D, respectively. Analysis of PFT coverage suggested that the study areas have spatially heterogeneous distributions of PFTs, based on the different polygonal morphologies. For example, for the with phenology classification, higher wet tundra graminoid values were predicted for Area A (Figure 6a) and lower moss values predicted for Area A (low centered polygons) (Figure 6b).

Figure 7 shows the average without phenology predicted PFT values for Areas A, B, C and D, which consists of 160,000 pixels. Results from the without phenology classification show PFT variability at both the polygon type and polygon feature scales. Mosses were predicted to have the highest coverage in Areas A, B, C and D with mean values of 42.1%, 44.8%, 50.5% and 60.9%, respectively. Wet tundra graminoids had the second highest coverage in Areas A, B, C and D with mean values of 30%, 26.6%, 27.1% and 27.9%, respectively. Bare ground had mean values of 14.7%, 12.9%, 12.4% and 15.9% for Areas A, B, C and D, respectively. Lichens had mean values of 9.7%, 13.3%, 7.3% and 1.4% for Areas A, B, C and D, respectively. Dry tundra graminoids had mean values of 6.2%, 8.5%, 6.4% and 2.1% for Areas A, B, C and D, respectively. Forbs had the lowest mean values of 4.4%, 6.1%, 8% and 7.3% for Areas A, B, C and D, respectively. Figure 8 shows the spatial distribution for each PFT estimation for the without phenology case.
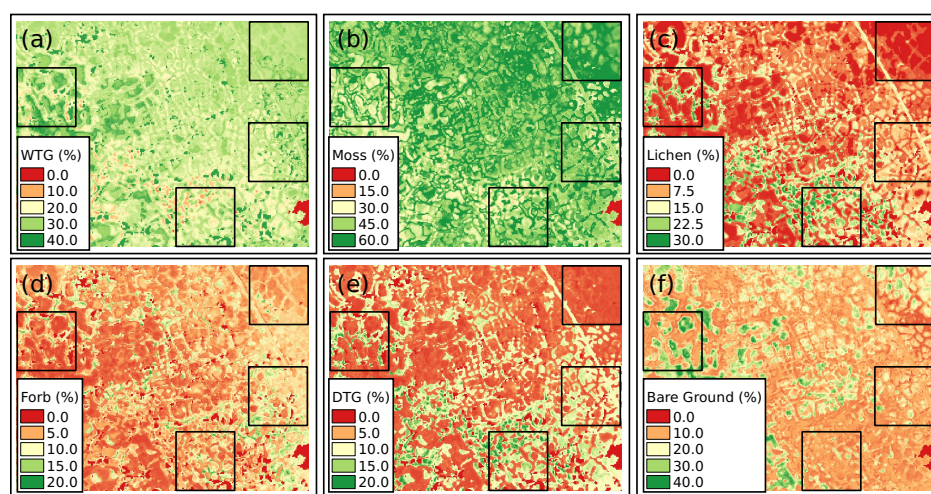


**Figure 6.** PFT estimation (%) for the with phenology case. The figure is structured as: (**a**) wet tundra graminoid estimation; (**b**) moss estimation; (**c**) lichen estimation; (**d**) forb estimation; (**e**) dry tundra graminoid estimation; and (**f**) bare ground estimation.
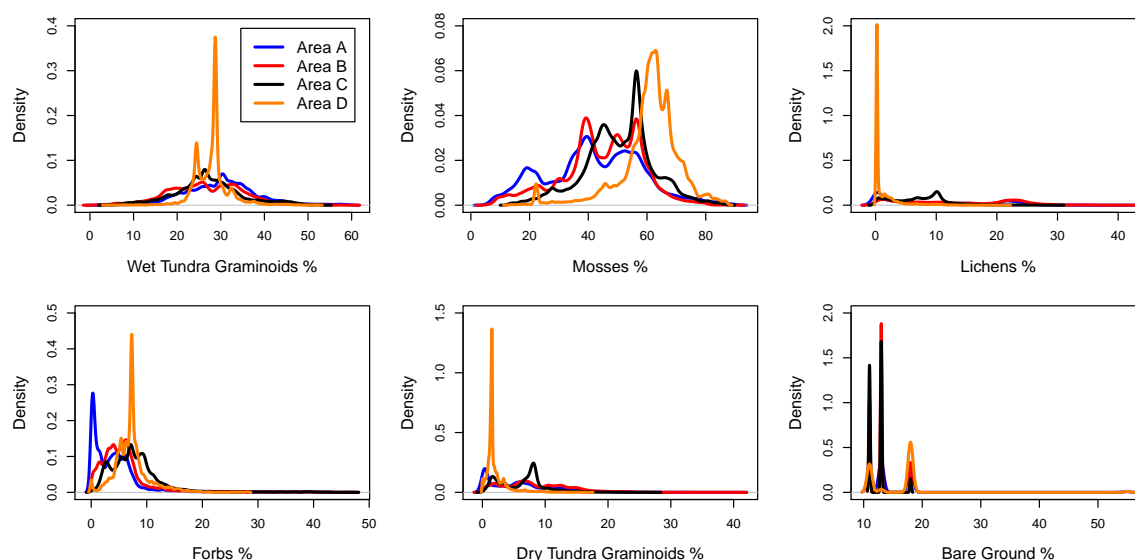


**Figure 7.** Distribution of PFTs for the without phenology classification from pixels within sampling Areas A (blue), B (red), C (black) and D (orange).
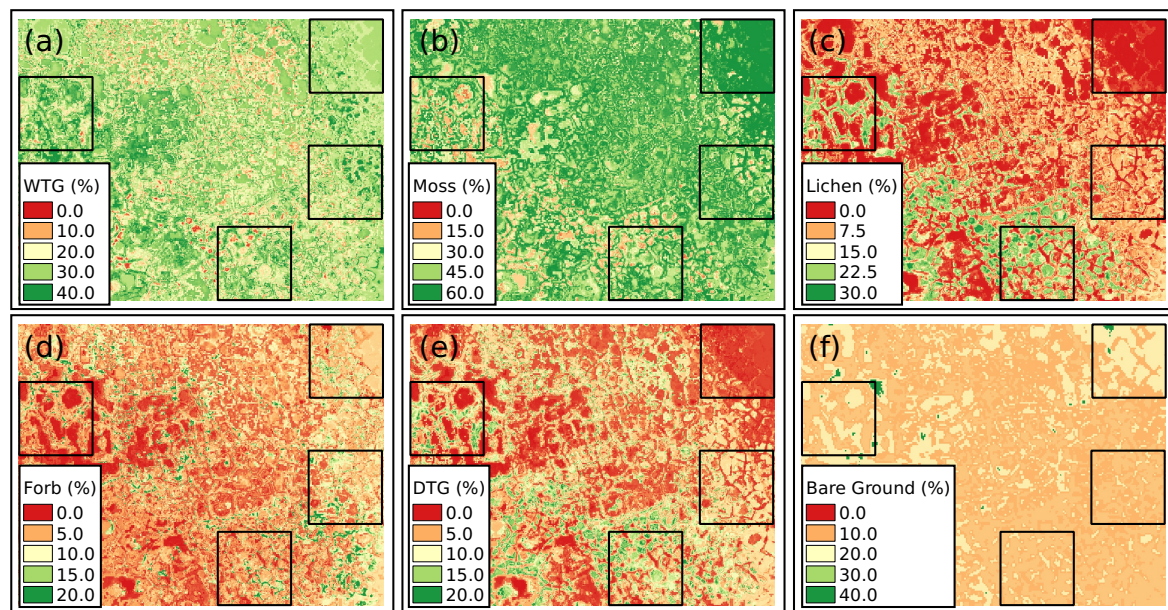
**Figure 8.** PFT estimation (%) for the without phenology case. The figure is structured as: (**a**) wet tundra graminoid estimation; (**b**) moss estimation; (**c**) lichen estimation; (**d**) forb estimation; (**e**) dry tundra graminoid estimation; and (**f**) bare ground estimation.

## 3.4. Validation of Upscaled PFT Distribution

### 3.4.1. Representativeness

Figure 9 shows the representativeness metric across the study Areas A, B, C and D for the without phenology (a) and with phenology (b) cases quantitatively representing how well the vegetation observations captured the variability in the multi-variate data space. The well-represented locations for Areas A, B, C and D had mean representativeness values of 1.71 and 0.35 for the with phenology and without phenology case, respectively. The under-represented locations for Areas A, B, C and D had mean representativeness values of 3.45 and 0.62 for the with phenology and without phenology case, respectively. The values of the representativeness metric for the without phenology case were lower because of the spectral similarities across data space when spectral data from a single date (i.e., six variables) during the growing season were used.
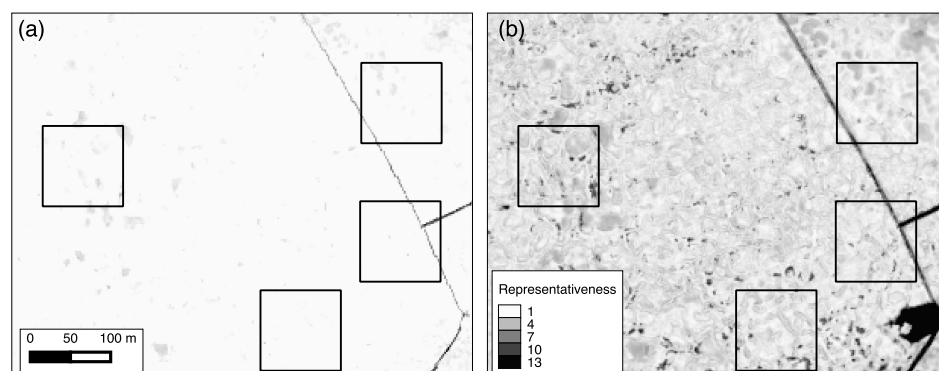


**Figure 9.** Representativeness of the vegetation samples across the study region for the (**a**) without phenology and (**b**) with phenology cases, with whiter colors indicating well-represented values and darker colors indicating under-represented areas.

To understand the difference in the estimated PFT distributions among two studied cases, difference maps were produced by subtracting the with phenology estimate from the without phenology estimate. Figure 10 shows the difference maps for moss (a) and wet tundra graminoid (b), with the greatest differences occurring in the under-represented areas (Figure 9b). Estimates of wet tundra graminoid and moss showed the greatest differences when including phenology, with mean absolute values of 5.9% and 7.9%, respectively. Forbs and dry tundra graminoids showed the lowest amount of difference, with mean absolute values of 2.7% and 3.2%, respectively. Lichens showed mean absolute differences of 4.1%.
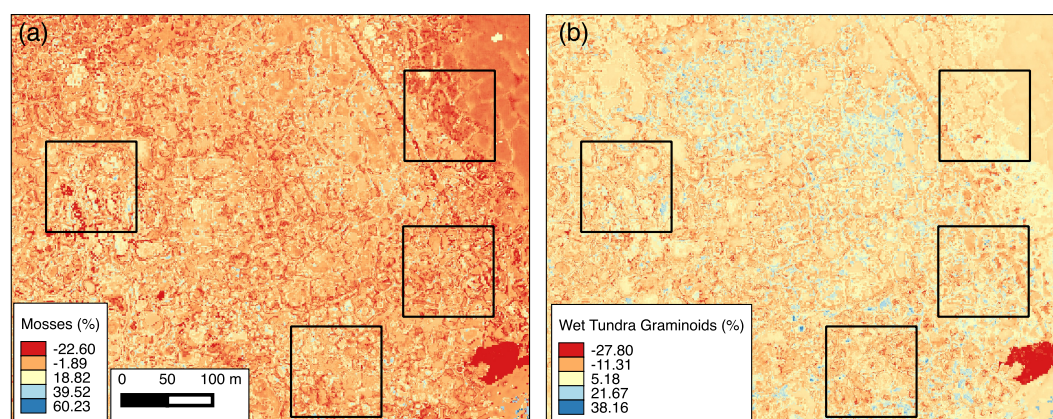
**Figure 10.** The difference from subtracting the with phenology and without phenology classifications of (**a**) mosses and (**b**) wet tundra graminoids.

### 3.4.2. Ground-Truthing of the Upscaled PFT Distribution

The representativeness metric was used for the selection of sites for field-based ground-truthing (as described in Section 2.5.2). The mean PFT distributions at ground-truthing locations were similar to the PFT values from field observations conducted in 2012, which were used to train/develop the IDW model. For example, the mean value for wet tundra graminoid for the ground-truthed data and input data into the IDW model was 25.9% and 30%, respectively. However, for some PFTs, the range of the ground-truthed data was not as large as the 2012 PFT values. This could be due to a few sampling plots that had a significant or less significant amount of PFT coverage.

Figure 11 shows the correlations and error statistics of the estimated PFT distributions for with phenology (a) and without phenology (b) cases (with all PFTs studies shown in different colors) compared against the 24 ground-truthed locations. The estimates from the with phenology case had better correlations and error statistics compared to the estimates from the without phenology case. The slight differences in PFT distributions for different years and fewer sampling locations used during ground-truthing could be one of the reasons why some PFTs perform better than others. Wet tundra graminoids and mosses had the best correlation with the ground-truthing data for the with phenology case, which represent a large part of the landscape (Table 5). We infer that including multiple images during the growing season (capturing phenology) led to a better upscaling when compared to the without phenology case. Phenology appears to help discriminate various PFTs through salient differences in timing and magnitude of spectral information, reflecting differences in the timing of blooming and green-up during the growing season.
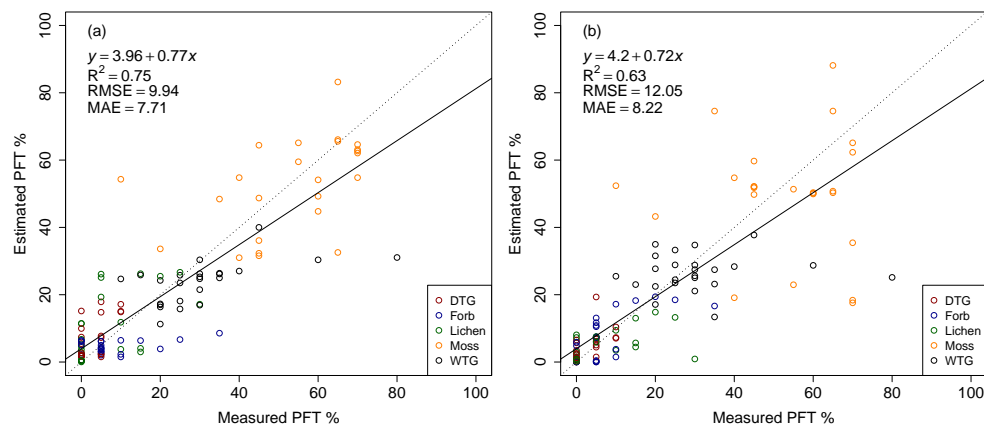
**Figure 11.** Model validation statistics for estimated PFTs compared to ground-truthing observations for the (**a**) with phenology and (**b**) without phenology case (DTG: dry tundra graminoids; WTG: wet tundra graminoids). Error indicators are *RMSE* (root mean squared error) and MAE (mean absolute error). The points are color coded by PFT; mosses are orange; lichens are green; forbs are blue; WTGs are black; and DTGs are red.

### 3.4.3. Improving Upscaling of PFTs Using Representativeness-Based Sampling

The 24 ground-truthing locations were selected using representativeness, thus collecting 12 samples in the regions that were poorly sampled by the initial vegetation samples. The observations from the ground-truthing campaign were thus added to the training set, and the IDW model for all of the PFTs for both the cases was recomputed. Including the 24 well- and under-represented ground-truthed sites (with the original PFT samples) in the IDW model improved the PFT estimation when performing the second ground-truthing campaign, with an $R^2 = 0.61$ compared to the original model with an $R^2 = 0.23$ (Figure 12). Mosses underestimate and wet tundra graminoids overestimate the ground-truthing when using the original model.
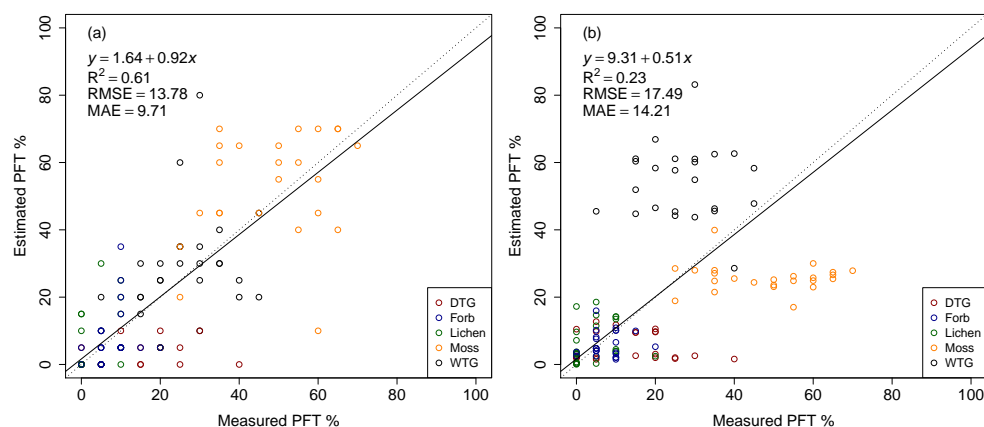


**Figure 12.** Model validation statistics for the (**a**) the improved model and (**b**) the original model for the case. Error indicators are *RMSE* and *MAE*. The points are color coded by PFT; mosses are orange; lichens are green; forbs are blue; WTGs are black; and DTGs are red.

While we focused our discussion on the Areas A, B, C and D, our PFT upscaling was conducted over a larger region for which LiDAR datasets were available. Figure 13 shows the density distribution of PFTs for Areas A, B, C and D (160,000 pixels) in comparison to that for the larger study region defined by the LiDAR data extent (94,070,288 pixels). The distribution of PFTs for Areas A, B, C and D was similar to that for the larger study domain (Figure 13). The distribution shows relatively

low proportions of lichens, dry tundra graminoids and forbs and high proportions of wet tundra graminoids and mosses. Wet tundra graminoids had a mean value of 26.5% for Areas A, B, C and D and the larger study domain, while mean values for mosses were 48.8% and 46.9%, respectively. Accurate PFT maps over a large area are vital when running high-resolution land surface models outside the sampling areas. This analysis could guide future field campaigns of vegetation sampling for extrapolating measurements over large areas in Arctic ecosystems. Our analysis indicates that including the representativeness analysis in the IDW model, by selecting sites that were not well represented, improved the estimated PFT distributions.
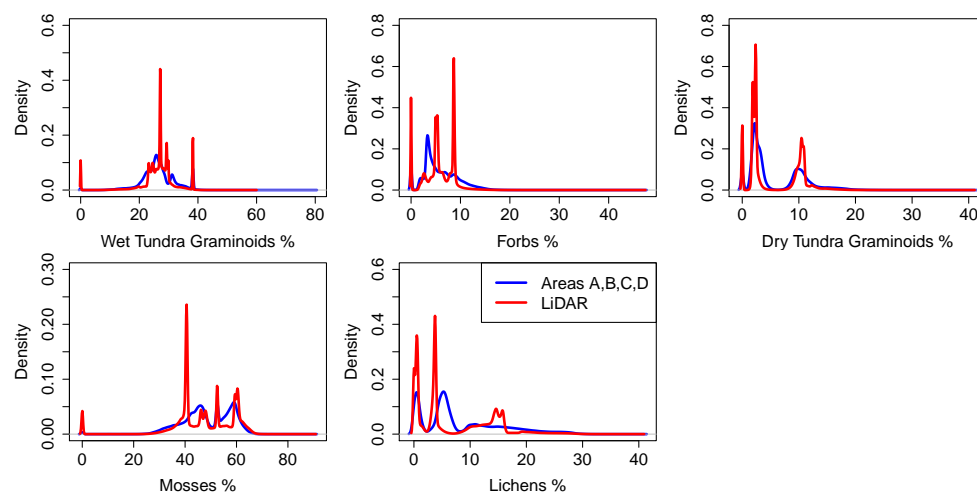


**Figure 13.** Density of PFT distributions using the improved model for Areas A, B, C and D (blue) and the larger study region (red).

## 4. Discussion

High-resolution LiDAR and optical datasets are becoming more accessible, and new approaches for analyzing such datasets are valuable to improving knowledge of Arctic ecosystems. This study estimated the distribution of PFTs using multiple high-resolution satellite imagery captured during the 2010 growing season. We developed an approach that combines *k*-means clustering [42], representativeness [31,43], and interpolation methods for optimally using the sparse point measurements to develop continuous gridded PFT estimates; taking a different approach from previous studies.

WorldView-2 multispectral satellite imagery has a much higher resolution compared to commonly-used satellites (e.g., Landsat, MODIS, etc.) and captures the fine-scale variation in PFTs within a small sampling domain. Clustering the spectral and topographic characteristics together provided a systematic method for delineating the landscape and allowed for the development of better upscaling models using field observations from similar environment (in the multi-variate data space). We conducted cluster analysis for varying level of divisions ($k = 3 \dots 10$) with the primary focus on stratifying the polygonal landscape. At our polygonal tundra sites with significant microtopography, cluster analysis at the $k = 6$ level of division provided the best stratification of the landscape (Figure 4) and provided the highest correlation coefficient during the bootstrap validation. For application to a different landscape, the optimal level (*k*) for clustering based stratification can be adjusted to appropriately capture the heterogeneity and features of interest.

Data from the vegetation surveys (mid-July 2012) and the first field ground-truthing campaign (late-July 2014) were very comparable, indicating similar vegetation conditions at the site during 2012 and 2014. The distribution of vegetation (PFTs) varies throughout the growing season, for example, early in the growing season standing biomass will be dominated by mosses and lichens, with the vascular plant component increasing as the season progresses [46]. Data indicate that

including multiple images during seasonal growth, thus capturing phenology, captured this variance in our upscaling model. Including the targeted field observations at well- and under-represented sites collected as part of field based validation significantly improved the accuracy of PFT estimates. However, the $R^2$ was lower for the with phenology case (Figure 12a) when compared to the first ground-truthing (Figure 11a) exercise. Data show that the second ground-truthing campaign was conducted in late-August 2014, while most the PFTs were beginning the "brown-down" period. Specifically, our with phenology IDW model captured the "green-up" period during the 2010 growing season, and sufficient remote sensing data were not available to capture the "brown-down" period. Including more remote sensing images during the last part of the growing season would help capture the "brown-down" and, therefore, potentially further distinguish PFT distributions. Including the whole growing season in the PFT estimate may help represent dynamic PFTs for models.

IDW works well with high-resolution remote sensing datasets; in addition, by stratifying the landscape using cluster analysis and developing separate model with each cluster and using the observations within the cluster allowed for spectral similarity and, thus, better and specialized models. The results of this study are applicable to the regions with similar vegetation and spectral characteristics. Furthermore, this study is well suited for upscaling fine-scale measurements over areas similar to the BEO. For example, clouds may become an issue if one decides to study larger areas. However, the same approach could be applied to cloud-penetrating L-band Synthetic Aperture Radar or to a subset of imagery throughout the growing season.

The distribution of PFTs for Areas A, B, C and D shows a multimodal distribution, which could be due to the polygonal types and features and was also attributable to how observers estimated plant distributions by multiples of 5% or 10% (Figure 13). For example, higher wet tundra graminoid values were predicted for Area A (low centered polygons), while lower wet tundra graminoid values were predicted for Area B (high centered polygons). This attribution of microtopography can also be seen in other upscaling studies around Barrow, AK [27]. For Arctic landscapes where the polygonal landscape are not the primary control, PFTs could depend on other criteria, such as the topographic position, and it is essential to find specific algorithms and model parameters with proper site-specific PFT measurements.

The Euclidean distance in the multi-variate state space provided a metric for representativeness. Gray-scaled representativeness maps showed the similarity of every map cell to the vegetation sampling locations in the BEO. This provided a sampling strategy to identify under-represented areas for further field sampling. Including additional observations from the under-represented areas in the IDW model significantly improved the estimation of PFT distributions across the landscape. This analysis can provide model-inspired insights into optimal sampling strategies across space and through time [31]. The accuracy of the upscaled data were higher for areas well represented by the sampling sites and lower for areas that were under-represented. The difference maps from subtracting the with phenology and without phenology showed that the greatest differences occur in the poorly-represented areas (Figure 10). These poorly-represented areas are due to differences in the spectral and topographic differences, meaning that different vegetation characteristics could occur in these areas. Furthermore, highly saturated areas could produce under-represented areas, and adding moisture content to the upscaling approach could improve PFT estimates. The improved representativeness analysis still shows locations that are under-represented and should be investigated in future field campaigns.

The methods we utilized here have improved our ability to predict the vegetation cover across broad portions of the landscape on the BEO. On-going research to improve the relationships among species-specific tundra vegetation cover, biomass and the allocation of carbon below-ground to the production of roots and rhizomes [47,48] may extend the utility of remote-sensing from observable plant and environmental characteristics to unobservable characteristics and processes beneath the soil surface. Other Arctic landscapes could benefit from our research by gathering the measurements mentioned above and applying these methods (i.e., representativeness, clustering, interpolation).

However, one might want to test different multivariate statistical methods (i.e., linear regression, neural networks).

The remote sensing imagery was collected in 2010; the training data used were collected in 2012; and the ground-truthing was conducted in 2014. Changes in vegetation composition and cover do occur through time, but they are much slower in the Arctic tundra compared to other parts of the world [20]. However, herbivory outbreaks can occur in the BEO. Villarreal et al. [49] saw low amounts of biomass in 2008 for all communities caused by a lemming population outbreak. We are assuming that dramatic changes in PFT percentages did not occur for 2010, 2012 and 2014, since we had high coefficients of determination from the ground-truthing campaigns. In order to accurately verify this, more high-resolution satellite and aerial imagery would be needed for these years.

Terrestrial vegetation plays an important role in the dynamics of the Earth system through water and energy exchange and is a large source of uncertainty in models. Chapin et al. [13] recommended the use of Arctic- and boreal-specific PFTs in vegetation models, which includes deciduous shrubs, evergreen shrubs, sedges, grasses, forbs, *Sphagnum* moss, non-*Sphagnum* moss and lichens. Estimates of PFT distribution from our study provide necessary inputs to model vegetation across larger landscapes for high-resolution land surface models (e.g., Arctic Terrestrial Simulator, PFLOTRAN). Efforts are underway to perform model simulations at the BEO and to assess the sensitivity of including these Arctic-specific PFT distributions. The presented approach for upscaling in situ measurements using high-resolution satellite imagery provides a framework for future studies focusing on Arctic ecosystem change.

## 5. Conclusions

We presented a method for upscaling of the field-based observation of PFT distributions at a polygonal tundra site using high-resolution spectral remote sensing. Maps of Arctic PFT types in the tundra ecosystem at 0.25-m spatial resolution developed in this study are the most detailed and high resolution PFT distribution product as per our knowledge. The results and analysis presented support our hypothesis that the phenological pattern captured by the remote sensing helps improve the accuracy of the upscaling algorithm. Phenology helps discriminate the vegetation types by their blooming and green-up behavior throughout the growing season. The developed method was demonstrated to perform well for the upscaling of sparse observations. Landscape characterization helped stratify the heterogeneous landscape and allowed for the upscaling of the observation to areas with similar properties and an accurate upscaling model. The representativeness metric employed in the study provided a way to measure dissimilarity in pixels and provides an approach for optimal sampling design to reduce the uncertainties (Figure 12). This method takes a different approach than previous studies due to the high spatial and spectral resolution of the WorldView-2 and the covariation of vegetation with topography as captured by LiDAR-derived DEMs. Unlike previous studies, we developed and applied a data analytic approach using high spectral and spatial resolution WorldView-2 and LiDAR datasets to upscale the field-based observations of PFT distributions. It offers an approach for upscaling of sparse field observations using increasingly available rich high-resolution remote sensing datasets.

provide public access to these results of federally-sponsored research in accordance with the DOE Public Access Plan (http://energy.gov/downloads/doe-public-access-plan).

## Appendix

Provided here is a description of possible surface water conditions within the WorldView-2 satellite images and impacts on the IDW model. No in situ estimates for surface water conditions during the 2012 vegetation sampling campaign or for the 2010 WorldView-2 images were recorded. For inundated areas in the sampling plots, the observed PFT fraction included the vegetation above and below the surface water. The normalized difference surface water index (NDSWI) was used to estimate surface water conditions for the 2010 WorldView-2 images used for the with phenology case and one image on 19 July 2012, a period during the vegetation sampling time (Figure A1). NDSWI is a proxy of water table height and works in shallow water bodies [50]. A few images in the with phenology case (24 June 2010, 21 July 2010 and 26 July 2010) were possibly inundated with high NDSWI values. This is especially true for Area A and Area D dominated by the low center polygons. The image on 19 July 2012 looks dry with low NDSWI values, which corresponds to the visual estimates and photographs made in the field around this time (Figure 3d). The IDW upscaling model was applied using the 19 July 2012 WorldView-2 spectral characteristics to estimate the PFT distribution. The ground-truthing dataset, used in the manuscript, was applied to these PFT distributions, and the correlation coefficient was lower ($R^2 = 0.69$) than the with phenology PFT distributions. Furthermore, the $R^2$ values in the wet sampling areas (A and D) were higher (0.85 and 0.72, respectively) in the with phenology case compared to the 19 July 2012 image (0.75 and 0.68, respectively).
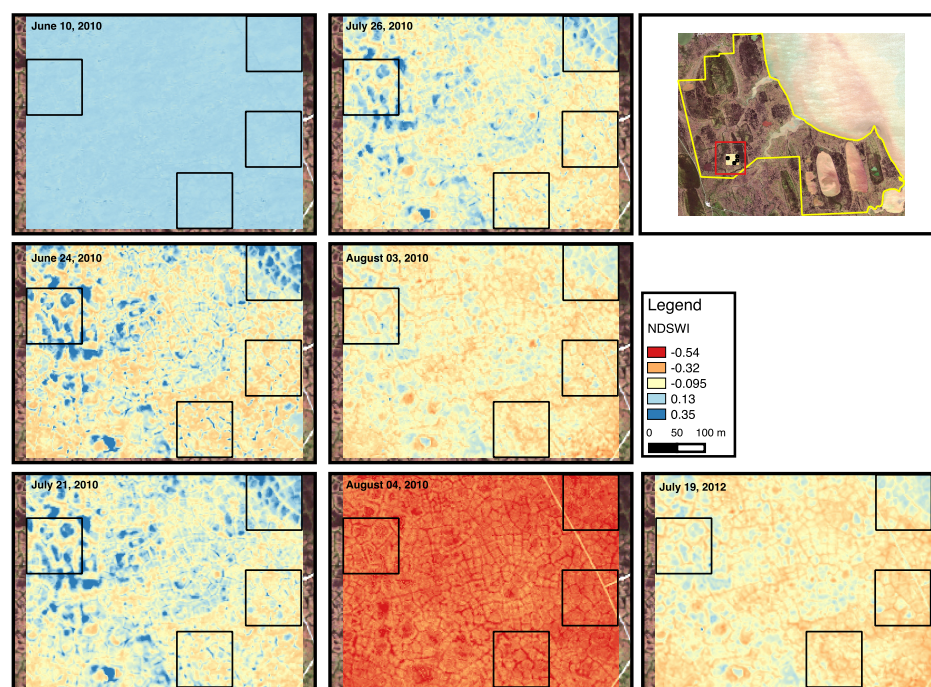


**Figure A1.** NDSWI values for Areas A, B, C and D for 2010 WorldView-2 images (10 June, 24 June, 21 July, 26 July, 3 August and 4 August) and one WorldView-2 image in 19 July 2012.

## References

1. Intergovernmental Panel on Climate Change (IPCC). Summary for policymakers. In *Climate Change 2013: The Physical Science Basis*; Contribution of Working Group I to the Fifth Assessment Report of the Intergovernmental Panel on Climate Change; Stocker, T., Qin, D., Plattner, G.K., Tignor, M., Allen, S., Boschung, J., Nauels, A., Xia, Y., Bex, V., Midgley, P., Eds.; Cambridge University Press: Cambridge, UK; New York, NY, USA, 2013.

2. Anisimov, O.A.; Vaughan, D.G.; Callaghan, T.V.; Furgal, C.; Marchant, H.; Prowse, T.D.; Vilhjálmsson, H.; Walsh, J.E. Polar regions (Arctic and Antarctic). In *Climate Change 2007: Impacts, Adaptation and Vulnerability*; Parry, M.L., Canziani, O.F., Palutikof, J.P., van der Linden, P.J., Hanson, C.E., Eds.; Cambridge University Press: Cambridge, UK, 2007; pp. 653–685.

3. Jorgenson, M.T.; Shur, Y.L.; Pullman, E.R. Abrupt increase in permafrost degradation in Arctic Alaska. *Geophys. Res. Lett.* **2006**, *33*, L02503.

4. Rowland, J.; Jones, C.; Altmann, G.; Bryan, R.; Crosby, B.; Hinzman, L.; Kane, D.; Lawrence, D.; Mancino, A.; Marsh, P.; et al. Arctic landscapes in transition: Responses to thawing permafrost. *Eos Trans. AGU* **2010**, *91*, 229–236.

5. Hinzman, L.; Deal, C.J.; McGuire, A.D.; Mernild, S.H.; Polyakov, I.V.; Walsh, J.E. Trajectory of the Arctic as an integrated system. *Ecol. Appl.* **2013**, *23*, 1837–1868.

6. Myers-Smith, I.H.; Forbes, B.C.; Wilmking, M.; Hallinger, M.; Lantz, T.; Blok, D.; Tape, K.D.; Macias-Fauria, M.; Sass-Klaassen, U.; Lèvesque, E.; et al. Shrub expansion in tundra ecosystems: Dynamics, impacts and research priorities. *Environ. Res. Lett.* **2011**, *6*, 045509.

7. Euskirchen, E.S.; Edgar, C.W.; Turetsky, M.R.; Waldrop, M.P.; Harden, J.W. Differential response of carbon fluxes to climate in three peatland ecosystems that vary in the presence and stability of permafrost. *J. Geophys. Res. Biogeosci.* **2014**, *119*, 1576–1595.

8. Wullschleger, S.D.; Epstein, H.E.; Box, E.O.; Euskirchen, E.S.; Goswami, S.; Iversen, C.M.; Kattge, J.; Norby, R.J.; van Bodegom, P.M.; Xu, X. Plant functional types in earth system models: Past experiences and future directions for application of dynamic vegetation models in high-latitude ecosystems. *Ann. Bot.* **2014**, *114*, 1–16.

9. Oleson, K.W.; Lawrence, D.M.; Bonan, G.B.; Drewniak, B.; Huang, M.; Koven, C.D.; Levis, S.; Li, F.; Riley, W.J.; Subin, Z.M.; et al. *Technical Description of Version 4.5 of the Community Land Model (CLM)*; NCAR Technical Note NCAR/TN-503+STR; National Center for Atmospheric Research: Boulder, CO, USA, 2013.

10. Smith, T.M.; Shugart, H.H.; Woodward, F.I. *Plant Functional Types: Their Relevance to Ecosystem Properties and Global Change*; Cambridge University Press: Cambridge, UK, 1997; p. 388.

11. Sun, W.; Liang, S.; Xu, G.; Fang, H.; Dickinson, R. Mapping plant functional types from MODIS data using multi-source evidential reasoning. *Remote Sens. Environ.* **2008**, *112*, 1010–1024.

12. Chapin, F.S.; McGuire, A.D.; Ruess, R.W.; Hollingsworth, T.N.; Mack, M.C.; Johnstone, J.F.; Kasischke, E.S.; Euskirchen, E.S.; Jones, J.B.; Jorgenson, M.T.; et al. Resilience of Alaska's boreal forest to climatic change. *Can. J. For. Res.* **2010**, *40*, 1360–1370.

13. Chapin, F.S.; Bret-Harte, M.S.; Hobbie, S.E.; Zhong, H. Plant functional types as predictors of transient responses of Arctic vegetation to global change. *J. Veg. Sci.* **1996**, *7*, 347–358.

14. Poulter, B.; Ciais, P.; Hodson, E.; Lischke, H.; Maignan, F.; Plummer, S.; Zimmermann, N.E. Plant functional type mapping for Earth system models. *Geosci. Model Dev.* **2011**, *4*, 993–1010.

15. Huemmrich, K.; Gamon, J.; Tweedie, C.; Campbell, P.; Landis, D.; Middleton, M. Arctic tundra vegetation functional types based on photosynthetic physiology and optical properties. *IEEE J. Sel. Top. Appl. Earth Observ. Remote Sens.* **2013**, *6*, 265–275.

16. Ustin, S.L.; Gamon, J.A. Remote sensing of plant functional types. *New Phytol.* **2010**, *186*, 795–816.

17. Atchley, A.L.; Painter, S.L.; Harp, D.R.; Coon, E.T.; Wilson, C.J.; Liljedahl, A.K.; Romanovsky, V.E. Using field observations to inform thermal hydrology models of permafrost dynamics with ATS (v0.83). *Geosci. Model Dev.* **2015**, *8*, 2701–2722.

18. Kumar, J.; Collier, N.; Bisht, G.; Mills, R.T.; Thornton, P.E.; Iversen, C.M.; Romanovsky, V. Modeling the spatio-temporal variability in subsurface thermal regimes across a low-relief polygonal tundra landscape. *Cryosphere Discuss.* **2016**, 1–32.

19. Tang, G.; Yuan, F.; Bisht, G.; Hammond, G.E.; Lichtner, P.C.; Kumar, J.; Mills, R.T.; Xu, X.; Andre, B.; Hoffman, F.M.; et al. Addressing numerical challenges in introducing a reactive transport code into a land surface model: A biogeochemical modeling proof-of-concept with CLM–PFLOTRAN 1.0. *Geosci. Model Dev.* **2016**, *9*, 927–946.

20. Stow, D.A.; Hope, A.; McGuire, D.; Verbyla, D.; Gamon, J.; Huemmrich, F.; Houston, S.; Racine, C.; Sturm, M.; Tape, K.; et al. Remote sensing of vegetation and land-cover change in Arctic Tundra Ecosystems. *Remote Sens. Environ.* **2004**, *89*, 281–308.

21. Selkowitz, D.J. A comparison of multi-spectral, multi-angular, and multi-temporal remote sensing datasets for fractional shrub canopy mapping in Arctic Alaska. *Remote Sens. Environ.* **2010**, *114*, 1338–1352.

22. Atkinson, D.M.; Treitz, P. Arctic ecological classifications derived from vegetation community and satellite spectral data. *Remote Sens.* **2012**, *4*, 3948.

23. Dalmayne, J.; Möckel, T.; Prentice, H.; Schmid, B.; Hall, K. Assessment of fine-scale plant species beta diversity using WorldView-2 satellite spectral dissimilarity. *Ecol. Inform.* **2013**, *18*, 1–9.

24. Ramoelo, A.; Cho, M.; Mathieu, R.; Madonsela, S.; van de Kerchove, R.; Kaszta, Z.; Wolff, E. Monitoring grass nutrients and biomass as indicators of rangeland quality and quantity using random forest modelling and WorldView-2 data. *Int. J. Appl. Earth Observ. Geoinform.* **2015**, *43*, 43–54.

25. Karna, Y.K.; Hussin, Y.A.; Gilani, H.; Bronsveld, M.; Murthy, M.; Qamer, F.M.; Karky, B.S.; Bhattarai, T.; Aigong, X.; Baniya, C.B. Integration of WorldView-2 and airborne LiDAR data for tree species level carbon stock mapping in Kayar Khola watershed, Nepal. *Int. J. Appl. Earth Observ. Geoinform.* **2015**, *38*, 280–291.

26. Mutanga, O.; Adam, E.; Cho, M.A. High density biomass estimation for wetland vegetation using WorldView-2 imagery and random forest regression algorithm. *Int. J. Appl. Earth Observ. Geoinform.* **2012**, *18*, 399–406.

27. Gangodagamage, C.; Rowland, J.C.; Hubbard, S.S.; Brumby, S.P.; Liljedahl, A.K.; Wainwright, H.; Wilson, C.J.; Altmann, G.L.; Dafflon, B.; Peterson, J.; et al. Extrapolating active layer thickness measurements across Arctic polygonal terrain using LiDAR and NDVI datasets. *Water Resour. Res.* **2014**, *50*, 6339–6357.

28. Richardson, A.D.; Keenan, T.F.; Migliavacca, M.; Ryu, Y.; Sonnentag, O.; Toomey, M. Climate change, phenology, and phenological control of vegetation feedbacks to the climate system. *Agric. For. Meteorol.* **2013**, *169*, 156–173.

29. Mills, R.T.; Kumar, J.; Hoffman, F.M.; Hargrove, W.W.; Spruce, J.P.; Norman, S.P. Identification and visualization of dominant patterns and anomalies in remotely sensed vegetation phenology using a parallel tool for principal components analysis. *Procedia Comput. Sci.* **2013**, *18*, 2396–2405.

30. Walker, J.; de Beurs, K.; Henebry, G. Land surface phenology along urban to rural gradients in the U.S. Great Plains. *Remote Sens. Environ.* **2015**, *165*, 42–52.

31. Hoffman, F.M.; Kumar, J.; Mills, R.T.; Hargrove, W.W. Representativeness-based Sampling Network Design for the State of Alaska. *Landsc. Ecol.* **2013**, *28*, 1567–1586.

32. Liljedahl, A.K.; Hinzman, L.D.; Harazono, Y.; Zona, D.; Tweedie, C.E.; Hollister, R.D.; Engstrom, R.; Oechel, W.C. Nonlinear controls on evapotranspiration in Arctic coastal wetlands. *Biogeosciences* **2011**, *8*, 3375–3389.

33. Bockheim, J.G.; Everett, L.R.; Hinkel, K.M.; Nelson, F.E.; Brown, J. Soil organic carbon storage and distribution in arctic Tundra, Barrow, Alaska. *Soil Sci. Soc. Am. J.* **1999**, *63*, 934–940.

34. Hubbard, S.; Gangodagamage, C.; Dafflon, B.; Wainwright, H.; Peterson, J.; Gusmeroli, A.; Ulrich, C.; Wu, Y.; Wilson, C.; Rowland, J.; et al. Quantifying and relating land-surface and subsurface variability in permafrost environments using LiDAR and surface geophysical datasets. *Hydrogeol. J.* **2013**, *21*, 149–169.

35. Brown, J. Tundra soils formed over ice wedges, Northern Alaska. *Soil Sci. Soc. Am. J.* **1967**, *31*, 686–691.

36. Washburn, A.L. *Geocryology: A Survey of Periglacial Processes and Environments*; The Blackburn Press: Caldwell, NJ, USA, 1978; p. 416.

37. Updike, T.; Comp, C. *Radiometric Use of WorldView-2 Imagery*; Technical Note; DigitalGlobe, Inc.: Longmont, CO, USA, 2010.

38. Rouse, J.; Haas, R.; Schell, J.; Deering, D. Monitoring vegetation systems in the Great Plains with ERTS-1. In Proceedings of the 3rd Earth Resources Technology Satellite Symposium, Washington, DC, USA, 10–14 December 1973; NASA: Washington, DC, USA, 1974; pp. 309–317.

39. Hartigan, J.A. *Clustering Algorithms*; John Wiley & Sons, Inc.: New York, NY, USA, 1975; p. 351.

40. Hoffman, F.M.; Hargrove, W.W.; Mills, R.T.; Mahajan, S.; Erickson, D.J.; Oglesby, R.J. Multivariate Spatio-Temporal Clustering (MSTC) as a data mining tool for environmental applications. In Proceedings of the iEMSs Fourth Biennial Meeting: International Congress on Environmental Modelling and Software Society (iEMSs 2008), Barcelona, Spain, 7–10 July 2008; pp. 1774–1781.

41. Bradley, P.S.; Fayyad, U.M. Refining initial points for *k*-means clustering. In Proceedings of the Fifteenth International Conference on Machine Learning (ICML 1998), Anaheim, CA, USA, 18–20 December 1998; Morgan Kaufmann Publishers Inc.: San Francisco, CA, USA, 1998; pp. 91–99.

42. Kumar, J.; Mills, R.T.; Hoffman, F.M.; Hargrove, W.W. Parallel *k*-Means clustering for quantitative ecoregion delineation using large datasets. In *Procedia Computer Science*, Proceedings of the International Conference on Computational Science (ICCS 2011), Singapore, 1–3 June 2010; Sato, M., Matsuoka, S., Sloot, P.M., van Albada, G.D., Dongarra, J., Eds.; Elsevier: Amsterdam, The Netherlands, 2011; Volume 4, pp. 1602–1611.

43. Hargrove, W.W.; Hoffman, F.M.; Law, B.E. New analysis reveals representativeness of the AmeriFlux Network. *Eos Trans. AGU* **2003**, *84*, 529–535.

44. Ringaby, E.; Friman, O.; Forssén, P.E.; Opsahl, T.; Haavardsholm, T.V.; Kåsen, I. Anisotropic scattered data interpolation for pushbroom image rectification. *IEEE Trans. Image Process.* **2014**, *23*, 2302–2314.

45. Dennis, J.G.; Tieszen, L.L.; Vetter, M.A. Seasonal dynamics of above- and below-ground production of vascular plants at Barrow, Alaska. In *Vegetation and Production Ecology of an Alaskan Arctic Tundra*; Springer: New York, NY, USA, 1978; Volume 29, pp. 113–140.

46. Huemmrich, K.; Gamon, J.; Tweedie, C.; Oberbauer, S.; Kinoshita, G.; Houston, S.; Kuchy, A.; Hollister, R.; Kwon, H.; Mano, M.; et al. Remote sensing of tundra gross ecosystem productivity and light use efficiency under varying temperature and moisture conditions. *Remote Sens. Environ.* **2010**, *114*, 481–489.

47. Sloan, V.; Brooks, J.; Wood, S.; Liebig, J.; Siegrist, J.; Iversen, C.; Norby, R. *Plant Community Composition and Vegetation Height, Barrow, Alaska, Ver. 1*; Next Generation Ecosystem Experiments Arctic Data Collection; Carbon Dioxide Information Analysis Center; Oak Ridge National Laboratory: Oak Ridge, TN, USA, 2014. Available online: http://dx.doi.org/10.5440/1129476 (accessed on 16 July 2012).

48. Iversen, C.M.; Sloan, V.L.; Sullivan, P.F.; Euskirchen, E.S.; McGuire, A.D.; Norby, R.J.; Walker, A.P.; Warren, J.M.; Wullschleger, S.D. The unseen iceberg: Plant roots in arctic tundra. *New Phytol.* **2015**, *205*, 34–58.

49. Villarreal, S.; Hollister, R.D.; Johnson, D.R.; Lara, M.J.; Webber, P.J.; Tweedie, C.E. Tundra vegetation change near Barrow, Alaska (1972–2010). *Environ. Res. Lett.* **2012**, *7*, 015508.

50. Goswami, S.; Gamon, J.A.; Tweedie, C.E. Surface hydrology of an arctic ecosystem: Multiscale analysis of a flooding and draining experiment using spectral reflectance. *J. Geophys. Res. Biogeosci.* **2011**, *116*, G00I07.

51. Langford, Z.; Kumar, J.; Hoffman, F. *Remote sensing-based characterization, 2-m, Plant Functional Type Distributions, Barrow Environmental Observatory, 2010*; Next Generation Ecosystem Experiments Arctic Data Collection; Carbon Dioxide Information Analysis Center; Oak Ridge National Laboratory: Oak Ridge, TN, USA, 2015. Available online: http://dx.doi.org/10.5440/1123668 (accessed on 16 July 2016).